

# Electrochemical properties of spinel $\text{Li}_4\text{Ti}_5\text{O}_{12}$ nanoparticles prepared via a low-temperature solid route

Mamoru Senna<sup>1,2</sup> · Martín Fabián<sup>1</sup> · Ladislav Kavan<sup>3</sup> ·  
Markéta Zukalová<sup>3</sup> · Jaroslav Briančin<sup>1</sup> · Erika Turianicová<sup>1</sup> ·  
Patrick Bottke<sup>4</sup> · Martin Wilkening<sup>4</sup> · Vladimír Šepelák<sup>1,5</sup>

Received: 12 April 2016 / Accepted: 31 May 2016 / Published online: 6 June 2016  
© Springer-Verlag Berlin Heidelberg 2016

**Abstract** Spinel phase  $\text{Li}_4\text{Ti}_5\text{O}_{12}$  (s-LTO) with an average primary particle size of 150 nm was synthesised via a solid state route by calcining a precursor mixture at 600 °C. The precursor was prepared from a stoichiometric mixture of  $\text{TiO}_2$  nanoparticles and an ethanolic solution of Li acetate and activated by ball-milling. Effects of the calcination temperature and atmosphere are examined in relation to the coexistence of impurity phases by X-ray diffraction and  $^6\text{Li}$  MAS NMR. The charge capacity of s-LTO, determined from cyclic voltammogram at a scan rate of 0.1 mV/s, was 142 mAh/g. The capacity of our optimised material is superior to that of commercially available spinel (a-LTO), despite the considerably smaller BET-specific surface area of the former. The superior properties of our material were also demonstrated by galvanostatic charging/discharging. From these observations, we conclude that the presented low-temperature solid state synthesis route provides LTO with improved electrochemical performance.

**Keywords**  $\text{Li}_4\text{Ti}_5\text{O}_{12}$  · Reactive precursor · Li-ion battery anode · Cyclic voltammetry · Impurity phases

✉ Mamoru Senna  
senna@applc.keio.ac.jp

<sup>1</sup> Institute of Geotechnics, Slovak Academy of Sciences, Kosice, Slovak Republic

<sup>2</sup> Faculty of Science and Technology, Keio University, Yokohama, Japan

<sup>3</sup> J. Heyrovsky Institute of Physical Chemistry, Academy of Sciences of the Czech Republic, Praha, Czech Republic

<sup>4</sup> Institute for Chemistry and Technology of Materials, Christian Doppler Laboratory for Lithium Batteries, Graz University of Technology, Graz, Austria

<sup>5</sup> Institute of Nanotechnology, Karlsruhe Institute of Technology, Karlsruhe, Germany

## Introduction

Spinel-type  $\text{Li}_4\text{Ti}_5\text{O}_{12}$  (LTO) is one of the most promising anode materials for lithium ion batteries [1–4] or capacitors [5, 6]. Preparation methods for LTO via a liquid phase are extensively discussed. They include solution [7], solvothermal [8], or sol-gel methods [9, 10]. Solid state preparation methods were adopted in many reports as reviewed in [11]. Well known drawbacks related to the low reactivity of the starting oxide mixture are associated with undesirable grain growth. Such drawbacks could be overcome by an increase in the nucleation site density and by subsequent crystal growth. Hence, a decrease in the diffusion path and an increase in the mobility of the diffusion species, i.e.  $\text{Li}^+$  ions have to be promoted. Such improvements in the reactants decrease the calcination temperature and hence the particle size. Smaller LTO particle size, in turn, improves the charging rate and hence is important for its application in Li-ion batteries [4]. Microwave irradiation is a unique alternative of the solid state synthesis [12]. From the viewpoint of affordable and scalable processes, however, we here exclude this option.

Minimising  $\text{TiO}_2$  particle size and mixing them as homogeneously as possible with a Li source are the key issues to increase the nucleation site density and to decrease the subsequent diffusion path for LTO crystal growth. Using a grinding mill seems to be appropriate for this purpose. Indeed, Zaghbi et al. used high-energy ball-milling to increase the reactivity of the starting mixture for LTO growth [13]. However, the mixture still required a heat treatment at 800 °C for 12 h to acquire phase purity. Excessive mechanical stress induces severe agglomeration of the reacting mixture suppressing the homogeneity of the reactants and hence increases the phase impurity of the products [14]. Therefore, a highly homogeneous precursor should be prepared without severe mechanical stressing

[15]. Following these concepts, we have recently developed a method to synthesise stoichiometric  $K_{0.5}Na_{0.5}NbO_3$  without any additives [16]. In such a case,  $K^+$  and  $Na^+$  competitively diffuse into  $Nb_2O_5$  [17], while  $Li^+$  ions solely diffuse into  $TiO_2$  during the crystallisation of LTO. Shin et al. studied the solid state processes of LTO by focusing on the role of the host oxides [18]. They used various  $TiO_2$  sources to prepare LTO and concluded that anatase nanoparticles are superior over rutile for product purity. They also emphasised the importance of the homogeneity of the reactant mixture. The stable intermediate,  $Li_2TiO_3$ , is preferentially formed when Li is locally accumulated throughout the overall stoichiometry of LTO. A similar conclusion was reported by Liu et al. by examining the positive effect of micronisation of titania, which was used as source material [19]. We have to note, however, that there are some opposite cases, where anatase is less desirable due to its phase transformation to rutile [18, 20–22].

The primary objective of this paper is to introduce a new preparation method of spinel type LTO nanoparticles via a solid state route, starting from a highly reactive, homogeneous reactant mixture. Emphasis is laid on the preparation of the starting mixture with the highest possible reactivity by using an ethanol solution of Li acetate as a Li source. The prepared LTO particles were characterised by several chemical and structural analyses and by potentiostatic and galvanostatic electrochemical measurements to examine their Li-insertion ability. By comparing these properties with those of commercial LTO, typical feature of the present preparation method was closed up.

## Materials and methods

### Synthesis of LTO powders

Lithium acetate,  $LiOCOCH_3$  (LiAc, Sigma-Aldrich), was dissolved in ethanol to obtain a 15 mass% ethanolic solution. An exact stoichiometric amount of  $TiO_2$  (Sigma-Aldrich, <25 nm particle size, anatase) was added to the LiAc solution to give ca 18.5 mass%  $TiO_2$ . The mixture was co-milled in a planetary mill (Pulverisette 6, Fritsch, Germany) at 150 rpm for 2 h by using a 250-mL vial and WC balls 10 mm in diameter. The ball-to-powder weight ratio was kept constant at 50:1. After co-milling, the resulted colloidal dispersion was dried in vacuum at approximately 70 °C overnight and subsequently at 195 °C in an ambient atmosphere for 5 h. After drying the mixture, the mechanically activated precursor (MAP) was obtained, which was then calcined in a tube furnace in air or under argon at a heating rate of 10 °C/min and held for 4 h up to a maximum temperature of 600 °C. One sample was calcined at 680 °C for comparison.

### Preparation of electrodes

A powder sample was dispersed in an aqueous medium to form a viscous paste. The powder (0.2 g) was mixed during stirring or gentle mortaring with 0.25 mL of 10 % aqueous solution of acetylacetone. Subsequently, 0.13 mL of 4 % aqueous solution of hydroxypropyl cellulose (Aldrich, MW 100,000) was added and finally 0.06 mL of 10 % aqueous solution of Triton X-100 (Fluka). Before use, the prepared slurry was homogenised by stirring. If the slurry was too viscous, it was further diluted by water. A titanium grid (5 × 15 mm, Goodfellow) was used as the electrode support. Electrodes were prepared by dip-coating. The coated area was ca 5 × 5 mm<sup>2</sup>. The prepared electrodes were dried in air, and finally calcined in air at 450 °C for 30 min.

### Characterisation

#### Solid state properties

Thermogravimetry and differential thermal analysis (TG-DTA) was carried out using a STA 449 F3 Jupiter apparatus (Netzsch, Germany). The sample, placed in an  $Al_2O_3$  crucible, was heated from room temperature up to 1000 °C in air at 10 °C/min.

Crystallographic properties were examined by powder X-ray diffraction (XRD) (Advance D8, Bruker, Germany, with Cu  $K\alpha$  radiation and accelerating voltage at 40 kV and 40 mA). XRD patterns were collected in the range of 15 to 70°  $2\theta$  with a step of 0.03°. Rietveld refinement of XRD data of the as-prepared sample after calcination was performed. XRD line broadening was analysed by the refinement of regular TCH-pV function parameters. In order to obtain a correct geometry set up and to eliminate instrumental broadening, an instrumental resolution function (IRF) was defined by refinement of  $LaB_6$  standard specimen.

Fourier transform infrared spectra (FTIR) were recorded on a Tensor 27 (Bruker, Germany) spectrometer in the range from 4000 to 380  $cm^{-1}$  with a spectral resolution of 4  $cm^{-1}$  and 64 scans. Raman spectra were measured by a Horiba, XploRA PLUS spectrometer with 532 nm diode laser excitation.

Particle size distribution was determined by dynamic light scattering (DLS) equipment comprising of a diode laser (Coherent Verdi V5 = 532 nm,  $P_{max} = 5$  W) and a goniometer. The signal was detected with single-mode fibre detection optics (OZ from GMP, Switzerland) acquired by a Perkin Elmer high-precision Photon Counting Module (Perkin Elmer, Canada) and an ALV 7002/USB Digital Multiple Tau Real Time Correlator (ALV, Germany). Light scattering was measured at a scattering angle of 90°. The corresponding size distribution function was calculated by the optimised regularisation technique [23]. Prior to measurements, powders

were dispersed in water and sonicated. Only the supernatant from the entire dispersion was collected for analysis. Hence, the particle size information relates to the ensemble of the smallest grains which occurred in the dispersion. BET surface area of the prepared materials was determined from nitrogen adsorption isotherms at 77 K (ASAP 2010, Micromeritics).

Microstructure and morphology were investigated using two electron microscopes, i.e. (i) a field emission-scanning electron microscope (FE-SEM, Mira 3, Tescan, Czech Republic) coupled with an EDS analyser (Oxford Instruments, UK) and (ii) a combined field emission (scanning) transmission electron microscope (S)TEM (JEOL JEM-2100F). Prior to the TEM investigations, the powders were crushed in a mortar, dispersed in ethanol, and fixed on a copper-supported carbon grid. UV spectra of samples were studied with a UV-Analytic JENA-Specord 250 Spectrophotometer by using an integrating sphere in the wavelength range of 200–700 nm.

$^6\text{Li}$  magic angle spinning (MAS) NMR spectra were recorded using a 500-MHz Avance III spectrometer (Bruker, Germany). We used a 2.5-mm rotor and a commercial MAS probe to acquire 1D MAS spectra at a 30-kHz spinning frequency with a single pulse excitation. The pulse length was about 2  $\mu\text{s}$ .

### Electrochemical properties

Electrochemical measurements were carried out in a one-compartment cell using an Autolab Pgstat-302N (Metrohm) controlled by GPES-4 software. The Li-insertion experiments were carried out in 1 M  $\text{LiPF}_6$  + ethylene carbonate (EC)/dimethylcarbonate (DMC) (1/1 by volume) in a glove box with an argon atmosphere. Reference and auxiliary electrodes were Li metal. Hence, the potentials are referred to as the  $\text{Li}/\text{Li}^+$  (1 M) reference electrode. Electrolytes, solvents, and redox-active molecules were of standard quality (p.a. or electrochemical grade) purchased from Aldrich or Merck and used as received.

Electrochemical impedance measurements were carried out using Autolab PGstat-30 equipped with the FRA module (Metrohm Autolab/Eco Chemie). Data were processed using Zview software (Scribner Associates, Inc). The impedance spectra were acquired in the frequency range from 100 kHz to 0.1 Hz, and at the voltage of 1.6 V vs.  $\text{Li}/\text{Li}^+$ , the modulation amplitude was 10 mV. The electrochemical cell, electrodes, and electrolyte solution were identical to those used in the other electrochemical experiments.

## Results and discussion

### Thermal analysis

As shown in Fig. 1, the DTA profile of the mixture (a) before and (b) after co-milling exhibited six endothermic peaks, A–F, upon heating in air up to 1000 °C. The main difference brought by co-

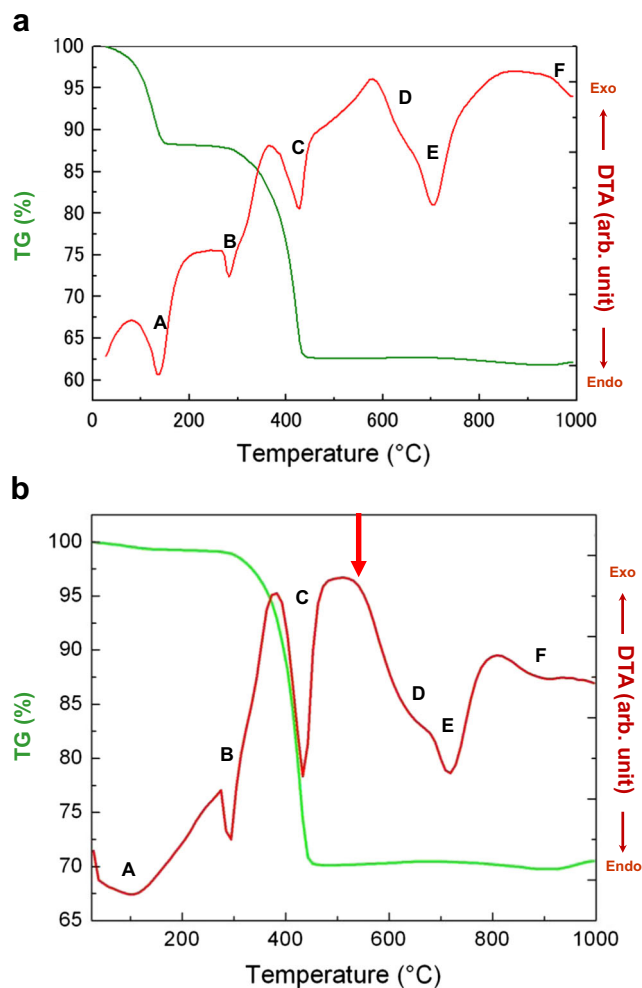


**Fig. 1** TG-DTA profile in the air for **a** the powder mixture and **b** MAP

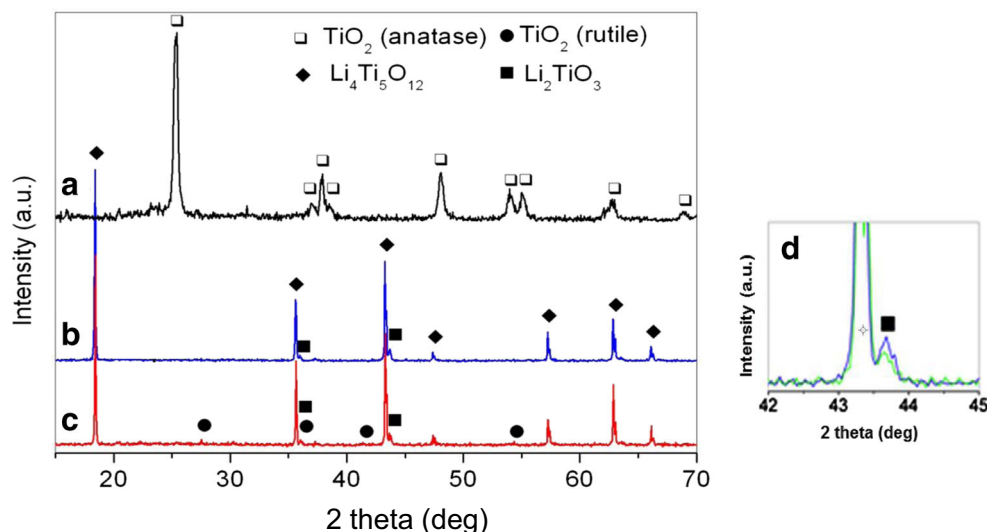
milling was the change at temperatures below 200 °C, where the removal of the rest of the solvent took place. The difference is mainly due to drying after milling, since a part of the solvent could be evaporated during co-milling. The sharp peaks B and C, observed at 300 and 440 °C, respectively, are accompanied by ca 30 % mass loss and are ascribed to the decomposition of the Li acetate to  $\text{LiCO}_3$  and subsequent decarbonisation [24]. The mass loss, slightly less than theoretical (35.6 mass%), might be attributed to the remaining  $-\text{OH}$  groups; this will be discussed below in conjunction with FTIR results.

The broad endothermic peaks, D and E (without weight loss), are attributed to the formation of  $\text{Li}_2\text{TiO}_3$  and the final product, LTO [25]. A comparison of the two TG profiles in Fig. 1a, b indicates that the starting temperature of the lithium titanate formation decreased by co-milling, i.e. from ca 580 to ca 530 °C, judging from the onset of the endothermic peak D.

### X-ray powder diffraction

Figure 2 shows representative XRD profiles of the precursor (MAP) (a) and the products obtained by isothermal treatments

**Fig. 2** X-ray diffractograms. **a** MAP and **b** calcined products in the air at 600 °C and **c** 680 °C and **d** 600 °C in the air (blue) and in Ar (green)



at 600 °C (b) and 680 °C (c). For MAP, we observe the diffraction peaks exclusively from anatase (JCPDS PDF 04-0477), i.e. no peaks from LiAc. The two calcined products exhibit almost exclusively the diffraction peaks ascribed to LTO (JCPDS PDF 72-0426) with a minute contribution from  $\text{Li}_2\text{TiO}_3$  (JCPDS PDF 33-0831) in both cases. For the sample calcined at 680 °C, we also observe very small peaks stemming from  $\text{TiO}_2$ , rutile (JCPDS PDF 86-0148). Appearance of the rutile phase might be explained as a result of the partial surface decomposition of LTO during cooling [26], while bulk decomposition is less probable since the eutectic temperature of LTO is reportedly 930 °C [27]. From these results, we assume that LTO can be obtained at temperatures as low as 600 °C. Therefore, MAP was calcined at 600 °C. Calcination was conducted either in air or in Ar. As shown in Fig. 2d, the content of  $\text{Li}_2\text{TiO}_3$  was slightly suppressed with the use of Ar. The calcined sample at 600 °C in argon is further labelled s-LTO, which was used for electrochemical characterisation.

The lattice constant,  $a$ , of s-LTO was 8.363 (4) Å, which is slightly larger than the typical values reported, i.e. between 8.33 and 8.36 Å [28, 29]. When LTO was prepared by hydrothermal growth for 10 h at 150 °C, the lattice constant increased from 8.33 to 8.37 Å. [9] The changes in lattice constant are known to be caused by, for example, the amount and distribution of oxygen vacancies as well as the associated partial reduction of  $\text{Ti}^{4+}$  to  $\text{Ti}^{3+}$ . Yi et al. [30] found that a larger lattice parameter is expected if some of the  $\text{Ti}^{4+}$  ions are transformed to  $\text{Ti}^{3+}$ , due to their larger size compared to  $\text{Ti}^{4+}$  ion. Note that the Pauling ionic radii are 68 nm for  $\text{Ti}^{4+}$  and 76 nm for  $\text{Ti}^{3+}$ . The mean crystallite size was found to be 128 nm.

### FTIR and Raman spectra

The FTIR spectra of MAP and its calcined products at 600 °C for 4 h in either air or in Ar are displayed in Fig. 3a. The FTIR

spectrum of MAP shows a stretching mode in the region 3600 to 3300  $\text{cm}^{-1}$ , corresponding to water molecules coordinated to lithium ions at different crystallographic sites [31] as well as hydrogen bonds on carboxylate ions [32]. The bands at 1730  $\text{cm}^{-1}$  (C=O stretching), 1582  $\text{cm}^{-1}$  (the most intense, C=O stretching), and 1432  $\text{cm}^{-1}$  (C=O stretching and C–O stretching, respectively) can be attributed to acetate ions [33, 34]. The characteristic stretching C–H modes are found at 3011  $\text{cm}^{-1}$  (–CH<sub>3</sub>) and 2933  $\text{cm}^{-1}$  (–CH<sub>2</sub>), respectively. The weak bands at 1348  $\text{cm}^{-1}$  (C–H bending), 1052  $\text{cm}^{-1}$  (C–H rocking), 1031  $\text{cm}^{-1}$  (C–H rocking), and 940  $\text{cm}^{-1}$  (C–C stretching) confirm the presence of aliphatic carbohydrates in the precursor. A small hump at 665  $\text{cm}^{-1}$  belongs to the OCO bending mode. The low-frequency part of the spectrum can be further characterised as overlapping of stretching Li–O (444  $\text{cm}^{-1}$ ) [34, 35] and Ti–O (500–600  $\text{cm}^{-1}$ ) [36] modes, respectively.

Calcination of MAP leads to the decomposition of organic parts in accordance with the results of thermal analysis. The FTIR spectrum shows a weak absorption band centred at around 3450  $\text{cm}^{-1}$ , due to –OH groups adsorbed on the surface of the calcined product. The O–H bending vibration centred at ca 1630  $\text{cm}^{-1}$  is most probably overlapped with the intensive C=O stretching band observed at 1582  $\text{cm}^{-1}$  [31]. The spinel vibrations at low wavenumbers, in the range of 400 to 700  $\text{cm}^{-1}$ , confirm LTO formation [37, 38]. Specifically, the low-frequency bands centred at 650 and 462  $\text{cm}^{-1}$  belong to symmetric and asymmetric stretching of  $\text{TiO}_6$  octahedra, respectively [39].

A closer look at the  $\text{TiO}_6$  stretching bands (Fig. 3b, c) does not reveal any difference between the samples calcined in air and Ar. For MAP, however, we observe clear doublet peaks between 600 and 700  $\text{cm}^{-1}$  (Fig. 3b). This is an indication of a change in the vibrational states of  $\text{TiO}_6$  by co-milling with LiAc.



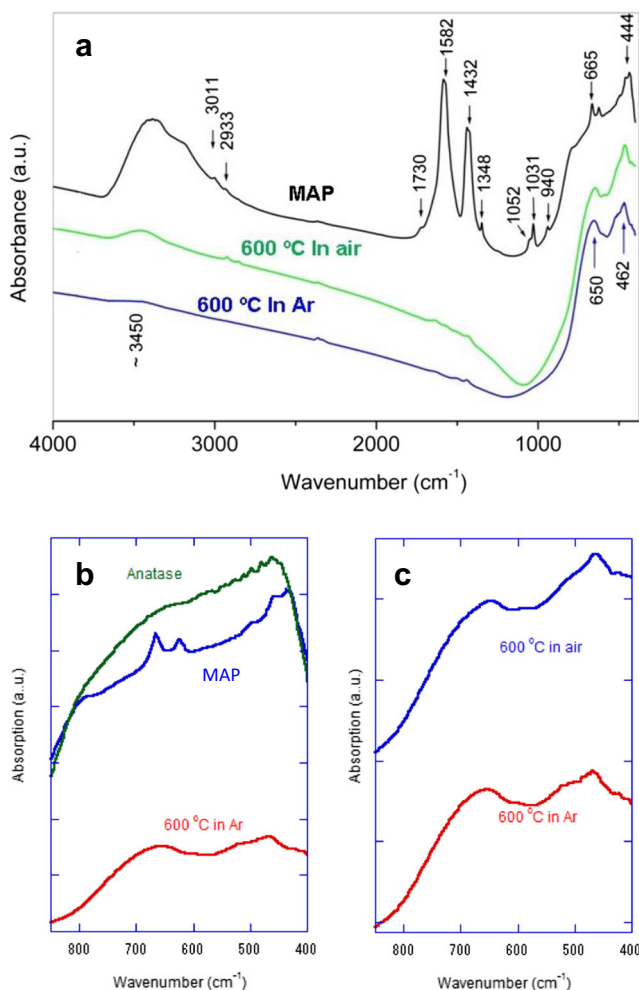


**Fig. 3** **a** FTIR spectra of MAP, and the sample calcined at 600 °C for 4 h in air and in Ar. **b, c** The detailed spectra for comparison

By comparing the Raman spectra, we observed almost identical spectra of anatase and the precursor as is shown in Fig. 4a. The observed bands can be ascribed

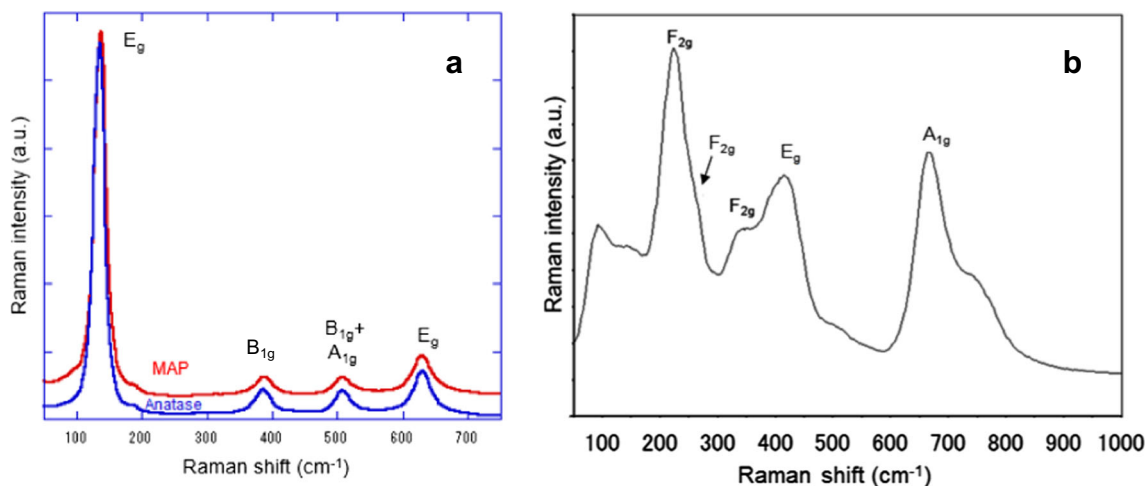


**Fig. 4** Raman spectra. **a** Anatase and MAP and **b** s-LTO

to those of anatase [40] which agrees with the XRD results discussed above. After calcination at 600 °C in Ar, i.e. in the s-LTO sample, the spectrum entirely changed (Fig. 4b). All the Raman bands for the calcined product agree well with those reported for phase pure LTO, i.e.  $A_{1g} + E_g + 3F_{2g}$  vibrational modes of the spinel phase [10, 41–44]. In agreement with earlier reports [45–47], we observe additional peaks, shown in Fig. 4b, which cannot be assigned to these fundamental modes. These unknown peaks are yet to be studied in conjunction with the phase purity. The absence of any peak in the region of the  $E_g(1)$  mode of anatase (at ca 144  $\text{cm}^{-1}$ ) is known to be a very sensitive indication that this impurity is not present [10]. Hence, our synthetic protocol provides a complete transformation of the  $\text{TiO}_2$  precursor to Li-titanates. This is a clear benefit over sol-gel synthesised LTO nanomaterials, which often contain anatase impurities [9, 10].

**UV-Vis diffuse reflectance spectra**

Starting with white anatase and LiAc, the precursor obtained after co-milling the mixture was brownish grey. The colour further changed by calcination to pale blue. This is in contrast to the white colour of the commercially available  $\text{Li}_4\text{Ti}_5\text{O}_{12}$ . A diffuse reflectance spectrum of the calcined product is shown in Fig. 5. The absorption between 600 and 700 nm corresponds to the colour observed. There are several reasons for the colouring of LTO, e.g. introduction of oxygen vacancies [26, 48] or reduction of  $\text{Ti}^{4+}$  to  $\text{Ti}^{3+}$  ions [49] as a consequence of co-milling, similar to the phenomena associated with partial lithiation, or hydrogenation [50]. A slight excess of Li, similar to lithiation of LTO, could also be responsible for this observation. This will be further discussed below.

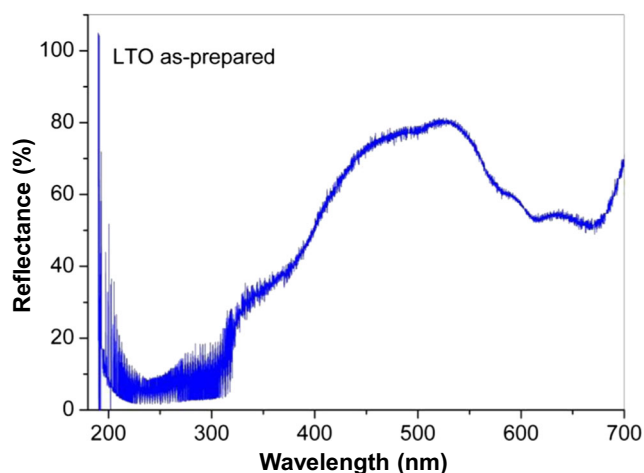


**Fig. 5** UV-Vis diffuse reflectance spectrum of s-LTO

### $^6\text{Li}$ MAS NMR

The  $^6\text{Li}$  MAS NMR spectrum of s-LTO is shown in Fig. 6a. The spectrum is composed of two main peaks which reflect Li ions distributed over octahedral 16d sites ( $-0.27(1)$  ppm) and tetrahedral 8a sites ( $0.08(1)$  ppm). Deconvolution of the spectrum of s-LTO shown in Fig. 6a using three Voigt functions is displayed in Fig. 6b. For ideal, fully stoichiometric  $\text{Li}_4\text{Ti}_5\text{O}_{12}$ , 75 % of the Li ions should reside on the 8a sites and 25 % on the 16d sites. The chemical shift values are in perfect agreement with those reported in the literature for LTO [51]. For the most intensive signal, the area under the NMR line is expected to be 75 %, provided the sample has ideal stoichiometry according to  $[\text{Li}]_{8a}[\text{Li}_{1/3}\text{Ti}_{5/3}]_{16d}[\text{O}_4]_{32e}$ . A value of 74.3 % is only slightly lower than the expected result for stoichiometric LTO. The signal at  $0.84(1)$  ppm likely reflects an impurity phase such as crystalline or amorphous

**Fig. 6 a**  $^6\text{Li}$  MAS NMR spectrum of s-LTO (spinning speed 30 kHz). Chemical shift (cs) values refer to aqueous LiCl. For comparison, the NMR spectrum of commercially available  $\text{Li}_2\text{TiO}_3$  (g-modification, Alfa Aesar) is also shown. **b** Deconvolution of the spectrum of the main portion of (a). See text for details

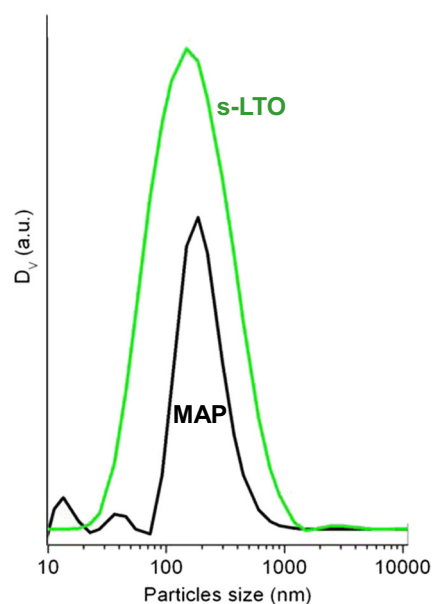
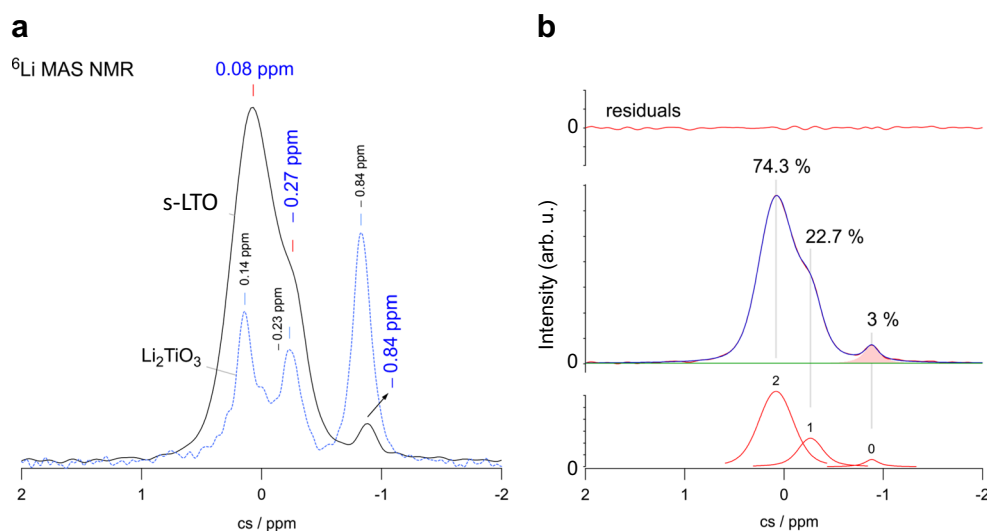


**Fig. 7** Particle size distribution profiles of MAP and s-LTO obtained from DLS

$\text{Li}_2\text{TiO}_3$ . Crystalline  $\text{Li}_2\text{TiO}_3$  was also detected in XRD (Fig. 2). Here, the amount of this extra phase is estimated to be below 3 % (see Fig. 6b). Note that in the  $\gamma$ -form of  $\text{Li}_2\text{TiO}_3$ , three magnetically inequivalent Li sites exist [52].

### Granulometrical analysis and morphological properties

Particle size distribution profiles obtained from the supernatant of the precursor, MAP and s-LTO sample by DLS are displayed in Fig. 7. The MAP consists of agglomerates with an average hydrodynamic diameter of about 184 nm. The presence of small particles in the range below 50 nm may

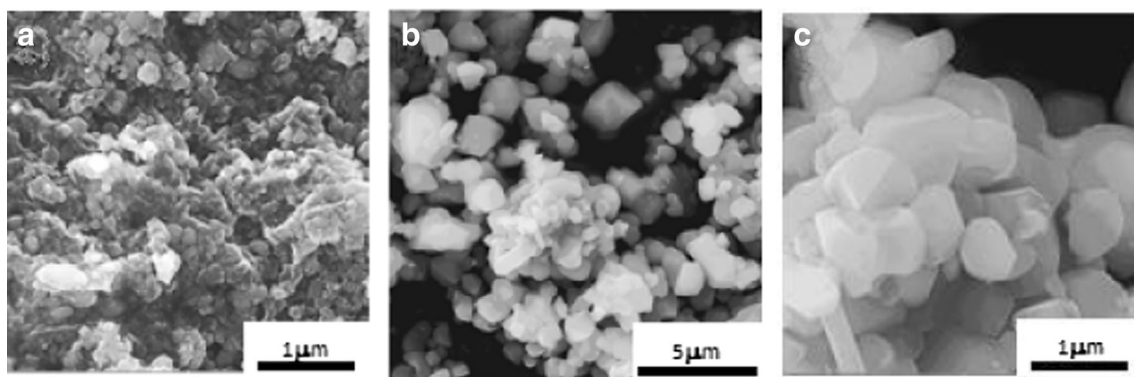


**Fig. 8** SEM images of **a** MAP and **b, c** s-LTO

probably be ascribed to anatase in the MAP. As described in “Materials and methods,” we have taken the supernatant of the dispersion of our samples after ultrasonication. The particles contained in the dispersion for the DLS measurement are, therefore, interpreted as being chipped debris from the agglomerated calcined powders, similar to the crystallite units. The peak of the hydrodynamic diameter from the supernatant was at around 150 nm. It is noteworthy that the observed peak size is in accordance with the mean crystallites size estimated by XRD analysis from s-LTO viz. ca 130 nm. From these observations, we may conclude that our product, s-LTO has its average crystallite size around 150 nm. The fairly small BET specific surface area, 1.4 m<sup>2</sup>/g, is an indication of particle growth in the as-calcined s-LTO powders, in spite of the calcination temperature being as low as 600 °C. This will be discussed below in conjunction with the electrochemical performance.

SEM images of our samples are shown in Fig. 8. A number of agglomerates of the nanoparticles are observed in MAP (Fig. 8a). On the other hand, s-LTO exhibits crystallised particles with partially developing crystalline habits (Fig. 8b, c). In a closer look at the particle morphology of s-LTO under TEM, we recognise the smallest particulate units with their average diameter close to those obtained from the supernatant of the s-LTO by DLS (ca 150 nm) and the crystallite size estimated from the X-ray diffractometry (ca 130 nm) (Fig. 9). The preservation of the crystallite size of MAP to the calcined crystallites in s-LTO seems to be one of the

benefits of the presented low-temperature solid state synthesis route, although we were not able to suppress grain growth completely. We also observe dense aggregated particles, in line with rather small BET specific surface area.

A systematic survey of particles size vs. BET surface areas of an array of LTO materials was presented in ref. [4]. From here, we can estimate that the surface area of s-LTO (1.4 m<sup>2</sup>/g) would be equivalent to a particle size of ca 1 μm. Analogously, the surface area of 12.5 m<sup>2</sup>/g found for the commercial sample, a-LTO (Aldrich) translates into ca order of magnitude smaller particle size, i.e. 0.1 μm.

### Electrochemical properties

The electrochemical performance of the sample s-LTO was evaluated by cyclic voltammetry of Li insertion (Fig. 10) and by galvanostatic chronopotentiometry at a charging/discharging current adjusted to 1C and 2C charging rate at a potential window 1.3–2.5 V vs. Li/Li<sup>+</sup> (Fig. 11). The charge capacity of s-LTO, determined from cyclic voltammogram at a scan rate of 0.1 mV/s was 142 mAh/g, calculated from the extraction branch of the cyclic voltammogram (Fig. 10). This is about 80 % of the theoretical capacity of phase pure Li<sub>4</sub>Ti<sub>5</sub>O<sub>12</sub>, 175 mAh/g [3]. The charge capacity of s-LTO significantly outperforms that of commercial lithium titanate, a-LTO, 95 mAh/g, despite the difference in the BET-specific surface area,  $S_{\text{BET}}$ , i.e. 1.4 and 12.5 m<sup>2</sup>/g, for s-LTO and a-LTO, respectively.

**Fig. 9** TEM images of s-LTO. Frames **(a)** and **(b)** are taken from the same specimen at different fields of view

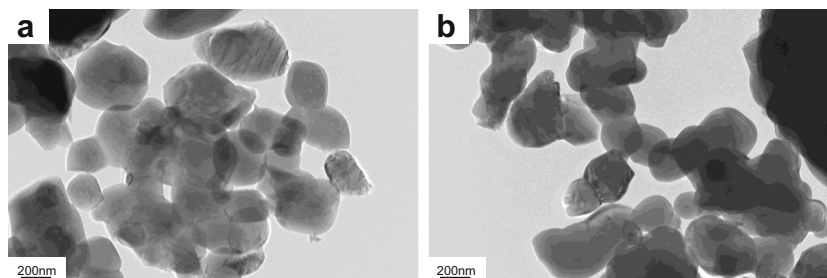
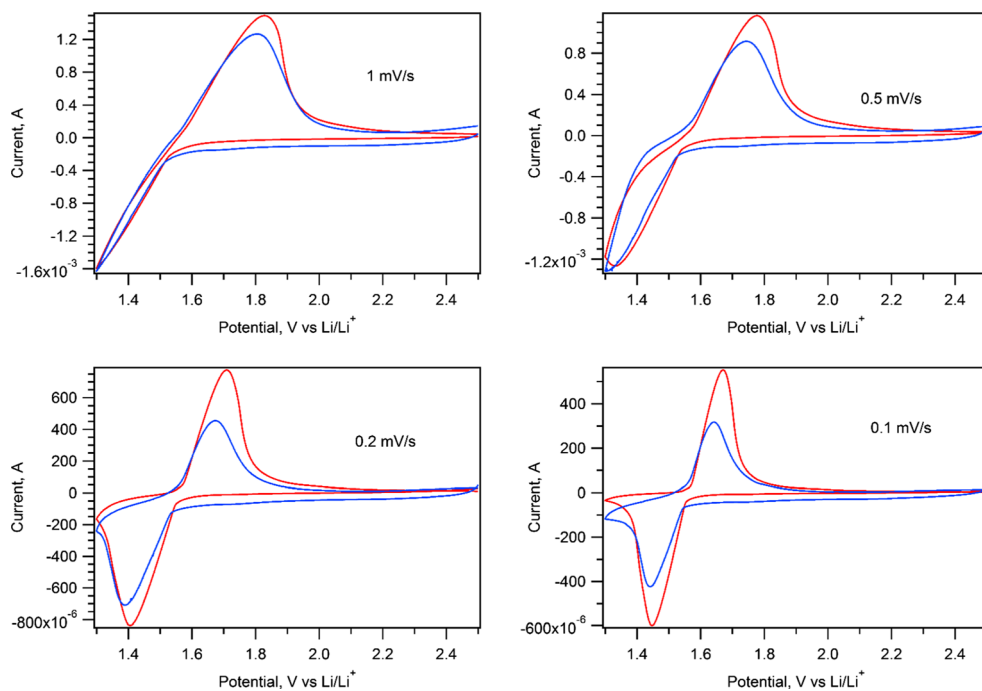


**Fig. 10** Cyclic voltammetry of Li insertion into s-LTO (red curve) and a-LTO (blue curve) at different scan rates. All curves are normalised with respect to the mass of active material on the electrode



Galvanostatic charging at the 1C rate (Fig. 11) provided s-LTO charge capacities of 116 mAh/g (charge) and 108 mAh/g (discharge) and at the 2C rate capacities of 65 mAh/g (charge) and 57 mAh/g (discharge). The performance of s-LTO is again better than that of a-LTO both at 1C charging rate (92 and 77 mAh/g for charging and discharging, respectively) and at 2C (39 and 35 mAh/g for charging and discharging, respectively), in spite of an almost order of magnitude smaller  $S_{\text{BET}}$  than that of a-LTO.

A sample s-LTO stability was evaluated by galvanostatic cycling at the 1C and 2C charging rates and compared with that of a-LTO sample (Fig. 12). For the sake of correctness, an initial capacity is in all cases calculated from the second cycle. The first cycle is considered to be a conditioning one, in which solid electrolyte interface (SEI) is formed. After 25 cycles at the 1C rate, a drop in capacity was 30 and 20 % for the s-LTO and a-LTO samples, respectively. Despite a larger capacity

drop of s-LTO sample, its nominal charge capacity after 25 cycles at the 1C rate is still comparable with the first cycle capacity of the a-LTO sample. At the 2C charging rate, the charge capacities of the s-LTO and a-LTO samples decreased after 25 cycles of about 9 and 16 %, respectively.

Figure 13 shows the electrochemical impedance spectra of a-LTO and s-LTO samples. The used working electrodes are FTO-supported thin films, free from any additives. The mass of active materials is 0.26 or 2.07 mg for a-LTO or s-LTO, respectively. Consequently, the total surface areas (calculated from the BET surface areas reported above) are roughly comparable: 35.2 or 29.0 cm<sup>2</sup>, for a-LTO or s-LTO electrodes, respectively. The impedance spectra and the corresponding fitted parameters are normalised with respect to the actual areas. Obviously, the high-frequency semicircle is ascribed to the charge-transfer resistance, and the low-frequency part is dominated by the Warburg impedance of semi-infinite

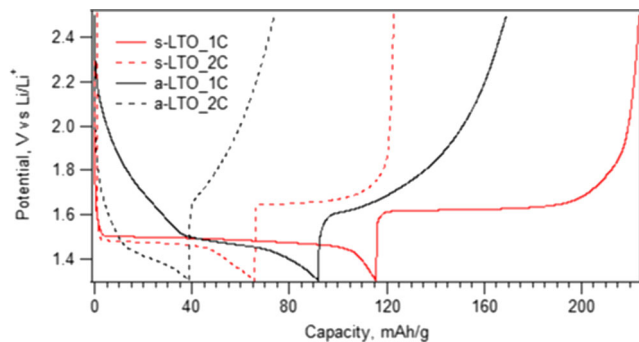


**Fig. 11** Galvanostatic chronopotentiometry of s-LTO and a-LTO at charging/discharging rates 1C and 2C

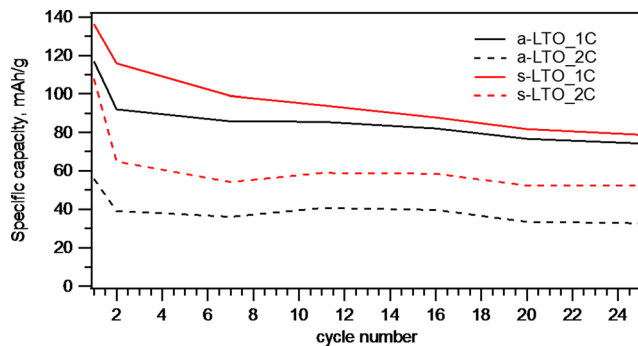


**Fig. 12** Galvanostatic cycling (25 cycles) of s-LTO and a-LTO at charging rates 1C and 2C



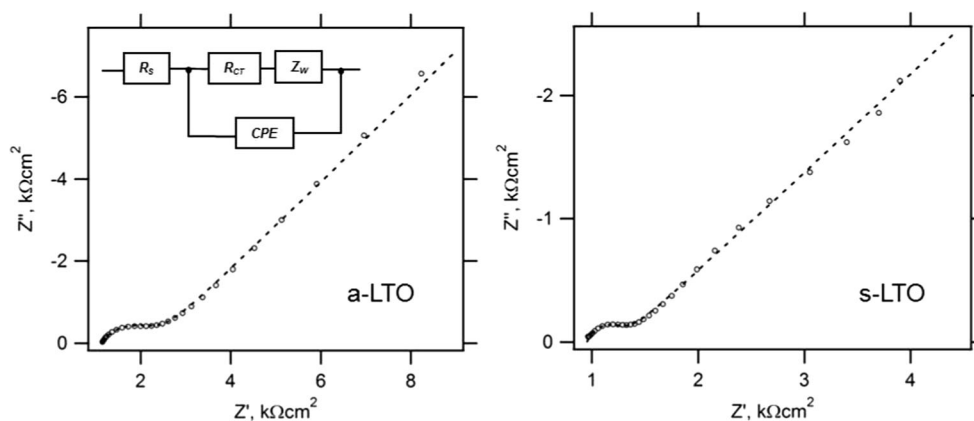


**Fig. 13** Nyquist plot of electrochemical impedance spectra measured at 1.6 V from 100 kHz to 0.1 Hz for the commercial reference material (a-LTO, left chart) and our synthesised sample (s-LTO, right chart). The spectra are normalised to the total (BET) surface area of the used

electrodes. *Inset* shows the equivalent circuit used for spectra fitting. The experimental points are represented by *markers* and the fitted spectra are displayed as *dashed lines*

diffusion of  $\text{Li}^+$ . The inset in the left chart shows the equivalent circuit used for fitting of experimental points. Here,  $R_S$  is the ohmic serial resistance,  $R_{CT}$  is the charge-transfer resistance,  $Z_W$  is Warburg impedance, and CPE the constant phase element describing deviation from the ideal capacitance. The impedance of constant phase element equals:  $Z_{CPE} = B(i\omega)^{-\beta}$  with  $B$ ,  $\beta$  being frequency-independent parameters of the CPE ( $0 \leq \beta \leq 1$ ). The fitted values of  $R_S$  are expectedly similar for both electrodes (1146 or 957  $\Omega\text{cm}^2$  for a-LTO or s-LTO, respectively). However, the fitted charge-transfer resistance is better for the s-LTO sample (319  $\Omega\text{cm}^2$ ) compared to a-LTO (609  $\Omega\text{cm}^2$ ). Obviously, the s-LTO material made by our optimised synthetic protocol is favoured over the reference commercial a-LTO by ca twice smaller charge-transfer resistance for Li insertion.

From these observations, we conclude that the presented material, s-LTO, is able to accommodate a higher quantity of Li ions compared to commercial a-LTO, in spite of an impurity phases content of around 3 % as estimated from  $^6\text{Li}$ -MAS NMR (Fig. 6). This is presumably due to the small average crystallite size at around 150 nm resulting from the low calcination temperature. Detailed examination, particularly in view of crystallography and associated local charge density distribution, is still needed to fully elucidate the difference between the two LTO samples. In this work, we have demonstrated interesting electrochemical performances from our calcined LTO.

## Conclusion

Spinel phase  $\text{Li}_4\text{Ti}_5\text{O}_{12}$  with an average crystallite size at around 150 nm was prepared via a solid state route by calcining a highly reactive precursor at 600 °C.  $^6\text{Li}$  MAS NMR indicates LTO with a Li site occupation which is near to that expected for  $\text{Li}_4\text{Ti}_5\text{O}_{12}$  with ideal stoichiometry. The charge

capacity of s-LTO determined from cyclic voltammogram at a scan rate of 0.1 mV/s was 142 mAh/g, which is about 80 % of theoretical capacity and is superior to commercially available LTO fine powders, despite having a smaller specific surface area of 1.4  $\text{m}^2/\text{g}$ . Superior electrochemical performance by s-LTO over a-LTO was also observed by galvanostatic charge/discharge. From these observations, we conclude that the presented low-temperature solid state synthesis of LTO provides highly active LTO material for applications in Li-ion batteries.

**Acknowledgments** This work was supported by V4-Japan Joint Research Program, Structure—function relationship of advanced monoxides for energy storage devices (AdOX) granted from Visegrad fund and Japan Science and Technology Agency. The partial financial support of VEGA (projects 2/0128/16, 2/0094/14 and 2/0064/14) and APVV (project 14-0103) is also acknowledged. The authors wish to thank to Dr. František Lofaj and Dr. Lenka Findoráková (Slovak Academy of Sciences, Slovakia) for Raman spectra and Dr. Angela Chemelli (TU Graz, Austria) for DLS experiments. M.W. would like to thank the Austrian Federal Ministry of Science, Research and Economy, and the National Foundation for Research, Technology and Development for the financial support. V.Š. thanks the support from DFG project (SE 1407/4-1). M.Z. acknowledges the financial support from the Grant Agency of the Czech Republic (15-06511S).

## References

1. Yi T-F, Jiang L-J, Shu J, Yue C-B, Zhu R-S, Qiao H-B (2010) Recent development and application of  $\text{Li}_4\text{Ti}_5\text{O}_{12}$  as anode material of lithium ion battery. *J Phys Chem Solids* 71:1236–1242
2. Zhang Q, Peng W, Wang Z, Li X, Xiong X, Guo H, Wang Z, Wu F (2013)  $\text{Li}_4\text{Ti}_5\text{O}_{12}$ /reduced graphene oxide composite as a high rate capability material for lithium ion batteries. *Solid State Ionics* 236: 30–36
3. Zaghbi K (1998) Electrochemistry of anodes in solid-state Li-ion polymer batteries. *J Electrochem Soc* 145:3135–3140
4. Kavan L, Procházka J, Spitzer TM, Kalbáč M, Zukalová M, Drenzel T, Grätzel M (2003) Li insertion into  $\text{Li}_4\text{Ti}_5\text{O}_{12}$  (spinel). *J Electrochem Soc* 150:A1000

5. Naoi K (2010) ‘Nanohybrid capacitor’: the next generation electrochemical capacitors. *Fuel Cells* 10:825–833
6. Zhu J, Zu W, Yang G, Song Q (2014) A novel electrochemical supercapacitor based on  $\text{Li}_4\text{Ti}_5\text{O}_{12}$  and  $\text{LiNi}_{1/3}\text{Co}_{1/3}\text{Mn}_{1/3}\text{O}_2$ . *Mater Lett* 115:237–240
7. Chiu H, Brodusch N, Gauvin R, Guerfi A, Zaghbi K, Demopoulos GP (2013) Aqueous synthesized nanostructured  $\text{Li}_4\text{Ti}_5\text{O}_{12}$  for high-performance lithium ion battery anodes. *J Electrochem Soc* 160: A3041–A3047
8. Xue Y, Wang Z, Yu F, Zhang Y, Yin G (2014) Ethanol-assisted hydrothermal synthesis of  $\text{LiNi}_{0.5}\text{Mn}_{1.5}\text{O}_4$  with excellent long-term cyclability at high rate for lithium-ion batteries. *J Mater Chem A* 2:4185
9. Kavan L, Grätzel M (2002) Facile synthesis of nanocrystalline  $\text{Li}_4\text{Ti}_5\text{O}_{12}$  (spinel) exhibiting fast Li insertion. *Electrochem Solid-State Lett* 5:A39
10. Kalbac M, Zukalova M, Kavan L (2003) Phase-pure nanocrystalline  $\text{Li}_4\text{Ti}_5\text{O}_{12}$  for a lithium-ion battery. *J Solid State Electrochem* 8: 2–6
11. Zhu G-N, Wang Y-G, Xia Y-Y (2012) Ti-based compounds as anode materials for Li-ion batteries. *Energy Environ Sci* 5:6652
12. Li J, Jin Y, Zhang X, Yang H (2007) Microwave solid-state synthesis of spinel  $\text{Li}_4\text{Ti}_5\text{O}_{12}$  nanocrystallites as anode material for lithium-ion batteries. *Solid State Ionics* 178(29–30):1590–1594
13. Zaghbi K, Simoneau M, Armand M, Gauthier M (1999) Electrochemical study of  $\text{Li}_4\text{Ti}_5\text{O}_{12}$  as negative electrode for Li-ion polymer rechargeable batteries. *J Power Sources* 81-82:300–305
14. Liao J-F, Senna M (1993) Mechanochemical dehydration and amorphization of hydroxides of Ca, Mg and Al on grinding with and without  $\text{SiO}_2$ . *Solid State Ionics* 66:313–319
15. Ando C, Suzuki T, Mizuno Y, Kishi H, Nakayama S, Senna M (2008) Evaluation of additive effects and homogeneity of the starting mixture on the nuclei-growth processes of barium titanate via a solid state route. *J Mater Sci* 43:6182–6192
16. Senna M, Pavlic J, Rojac T, Malic B, Kosec M, Brennecke G (2014) Preparation of phase-pure  $\text{K}_{0.5}\text{Na}_{0.5}\text{NbO}_3$  fine powders by a solid-state reaction at 625 °C from a precursor comprising  $\text{Nb}_2\text{O}_5$  and K, Na acetates. *J Am Ceram Soc* 97:413–419
17. Malic B, Jenko D, Holc J, Hrovat M, Kosec M (2008) Synthesis of sodium potassium niobate: a diffusion couples study. *J Am Ceram Soc* 91:1916–1922
18. Shin J-W, Hong C-H, Yoon D-H, Dudley N (2012) Effects of  $\text{TiO}_2$  starting materials on the solid-state formation of  $\text{Li}_4\text{Ti}_5\text{O}_{12}$ . *J Am Ceram Soc* 95:1894–1900
19. Liu W, Zhang J, Wang Q, Xie X, Lou Y, Han X, Xia B (2013) Microsized  $\text{TiO}_2$  activated by high-energy ball milling as starting material for the preparation of  $\text{Li}_4\text{Ti}_5\text{O}_{12}$  anode material. *Powder Technol* 247:204–210
20. Sun X, Radovanovic PV, Cui B (2015) Advances in spinel  $\text{Li}_4\text{Ti}_5\text{O}_{12}$  anode materials for lithium-ion batteries. *New J Chem* 39(1):38–63
21. Hong S-C, Hong H-P, Cho B-W, Na B-K (2010) Effect of heat treatment on electrochemical characteristics of spinel lithium titanium oxide. *Korean J Chem Eng* 27(1):91–95
22. Yuan T, Cai R, Gu P, Shao Z (2010) Synthesis of lithium insertion material  $\text{Li}_4\text{Ti}_5\text{O}_{12}$  from rutile  $\text{TiO}_2$  via surface activation. *J Power Sources* 195(9):2883–2887
23. Schnablegger H (1991) Optical sizing of small colloidal particles. *Appl Opt* 30(33):1889–1896
24. Shen CM (2002) Preparation and characterization of nanocrystalline  $\text{Li}_4\text{Ti}_5\text{O}_{12}$  by sol-gel method. *Mater Chem Phys* 78:437–441
25. Veljkovic I, Poleti D, Karanovic L, Zdujic M, Brankovic G (2011) Solid state synthesis of extra phase-pure  $\text{Li}_4\text{Ti}_5\text{O}_{12}$  spinel. *Sci Sinter* 43:343–351
26. Laumann A, Boysen H, Bremholm M, Fehr KT, Hoelzel M, Holzapfel M (2011) Lithium migration at high temperatures in  $\text{Li}_4\text{Ti}_5\text{O}_{12}$  studied by neutron diffraction. *Chem Mater* 23(11): 2753–2759
27. Hugo AM, Pfeiffer H (2011) Kinetic analysis of the thermal decomposition of  $\text{Li}_4\text{Ti}_5\text{O}_{12}$  pellets. *Process Appl Ceram* 5:199–203
28. Colbow KM, Dahn JR, Haering RR (1989) Structure and electrochemistry of the spinel oxides  $\text{LiTiO}_4$  and  $\text{Li}_{4/3}\text{Ti}_{5/3}\text{O}_4$ . *J Power Sources* 26:397–402
29. Ohzuku T, Ueda A, Yamamoto N (1995) Zero-strain insertion material of  $\text{Li}[\text{Li}_{1/3}\text{Ti}_{5/3}]\text{O}_4$  for rechargeable lithium cells. *J Electrochem Soc* 142:1431–1435
30. Yi T-F, Jiang L-J, Liu J, Ye M-F, Fang H-B, Zhou A-N, Shu J (2011) Structure and physical properties of  $\text{Li}_4\text{Ti}_5\text{O}_{12}$  synthesized at deoxidation atmosphere. *Ionics* 17:799–803
31. Barreto L-S, Mort K-A, Jackson R-A, Alves O-L (2002) Molecular dynamics simulations of anhydrous lithium acetate. *J Non-Cryst Solids* 303:281–290
32. Kearlay G-J, Nikolai B, Radelli P-G, Filleaux F (1996) The crystal structure and methyl group dynamics in the room-temperature and low-temperature phases of lithium acetate dihydrate. *J Solid State Chem* 126:184–188
33. Šurca Vuk A, Jovanovski V, Pollet-Villard A, Jenman I, Orel B (2008) Imidazolium-based ionic liquid derivatives for application in electrochromic devices. *Sol Energy Mater Sol Cells* 92:126–135
34. Zheng Z, Tang Z, Zhang Z, Shen W (2003) IR investigation and electrochemical properties of Li-doped spinel  $\text{Li}_{1+x}\text{Mn}_{2-x}\text{O}_4$  prepared by a simplified technique. *Russ J Electrochem* 39: 305–309
35. Meshitsuka S, Takashi H, Higashi K (1971) Infrared spectra and lattice vibrations of  $\text{Li}_2\text{SO}_4 \cdot \text{H}_2\text{O}$ . *Bull Chem Soc Jpn* 44:3255–3259
36. Gao Y, Masuda Y, Peng Z, Yonezawa T, Koumoto K (2003) Room temperature deposition of a  $\text{TiO}_2$  thin film from aqueous peroxotitanate solution. *J Mater Chem* 13:608–613
37. Zhang Q, Peng W, Wang Z, Li X, Xiong X, Guo H, Wang Z, Wu F (2012) Synthesis and characterization of  $\text{Li}_4\text{Ti}_5\text{O}_{12}$ /graphene composite as anode material with enhanced electrochemical performance. *Ionics* 19:717–723
38. Allen GCPM (1995) Chemical characterization of transition metal spinel-type oxides by infrared spectroscopy. *Appl Spectrosc* 49: 451–458
39. Raja MW, Mahanty S, Kundu M, Basu RN (2009) Synthesis of nanocrystalline  $\text{Li}_4\text{Ti}_5\text{O}_{12}$  by a novel aqueous combustion technique. *J Alloys Compd* 468:258–262
40. Frank O, Zukalova M, Laskova B, Kurti J, Koltai J, Kavan L (2012) Raman spectra of titanium dioxide (anatase, rutile) with identified oxygen isotopes (16, 17, 18). *Phys Chem Chem Phys* 14:14567–14572
41. Lin J-Y, Hsu C-C, Ho H-P, Wu S-h (2013) Sol-gel synthesis of aluminum doped lithium titanate anode material for lithium ion batteries. *Electrochim Acta* 87:126–132
42. Shimizu M, Usui H, Sakaguchi H (2016) Functional ionic liquids for enhancement of Li-ion transfer: the effect of cation structure on the charge-discharge performance of the  $\text{Li}_4\text{Ti}_5\text{O}_{12}$  electrode. *Phys Chem Chem Phys* 18:5139–5147
43. Zhu W, Zhuang Z, Yang Y, Zhang R, Lin Z, Lin Y, Huang Z (2016) Synthesis and electrochemical performance of hole-rich  $\text{Li}_4\text{Ti}_5\text{O}_{12}$  anode material for lithium-ion secondary batteries. *J Phys Chem Solids* 93:52–58
44. Yi T-F, Wu J-Z, Li M, Zhu Y-R, Xie Y, Zhu R-S (2015) Enhanced fast charge-discharge performance of  $\text{Li}_4\text{Ti}_5\text{O}_{12}$  as anode materials for lithium-ion batteries by Ce and  $\text{CeO}_2$  modification using a facile method. *RSC Adv* 5:37367–37376

45. Julien CM, Massot M, Zaghib K (2004) Structural studies of  $\text{Li}_{4/3}\text{Me}_{5/3}\text{O}_4$  (Me = Ti, Mn) electrode materials: local structure and electrochemical aspects. *J Power Sources* 136(1):72–79
46. Sinha MM, Gupta HC (2000) Study of phonons in superconducting oxide spinels  $(\text{Li, Mg})_{1+x}\text{Ti}_{2-x}\text{O}_4$ . *Phys Status Solidi B* 221:689–692
47. Kushwaha AK (2013) Lattice dynamical calculations for  $\text{Li}_{1+x}\text{Ti}_{2-x}\text{O}_4$  ( $x = 0.33$ ) and  $\text{Li}_{1-y}\text{Mg}_y\text{Ti}_2\text{O}_4$  ( $y = 0.1, 0.3$ ). *Acta Phys Pol A* 124:695–697
48. Dolotko O, Senyshyn A, Mühlbauer MJ, Boysen H, Monchak M, Ehrenberg H (2014) Neutron diffraction study of  $\text{Li}_4\text{Ti}_5\text{O}_{12}$  at low temperatures. *Solid State Sci* 36:101–106
49. Mukai K, Kato Y, Nakano H (2014) Understanding the zero-strain lithium insertion scheme of  $\text{Li}[\text{Li}_{1/3}\text{Ti}_{5/3}]\text{O}_4$ : structural changes at atomic scale clarified by Raman spectroscopy. *J Phys Chem C* 118(6):2992–2999
50. Qiu J, Lai C, Gray E, Li S, Qiu S, Strounina E, Sun C, Zhao H, Zhang S (2014) Blue hydrogenated lithium titanate as a high-rate anode material for lithium-ion batteries. *J Mater Chem A* 2:635
51. Kartha JP, Tunstall DP, Irvine JTS (2000) An NMR investigation of lithium occupancy of different sites in the oxide superconductor  $\text{LiTi}_2\text{O}_4$  and related compounds. *J Solid State Chem* 152:397–402
52. Ruprecht B, Wilkening M, Uecker R, Heitjans P (2012) Extremely slow Li ion dynamics in monoclinic  $\text{Li}_2\text{TiO}_3$  probing macroscopic jump diffusion via  $^7\text{Li}$  NMR stimulated echoes. *Phys Chem Chem Phys* 14:11974–11980